Tunability of interactions between the core and shell in rattle-type particles studied with liquid-cell electron microscopy

Tom A.J. Welling,[†] Kanako Watanabe,[‡] Albert Grau-Carbonell,[†] Joost de Graaf,[¶] Daisuke Nagao,[‡] Arnout Imhof,[†] Marijn A. van Huis,[*,†] and Alfons van Blaaderen[*,†]

[†]*Soft Condensed Matter, Debye Institute for Nanomaterials Science, Utrecht University, Princetonplein 5, 3584 CC Utrecht, The Netherlands*

[‡]*Department of Chemical Engineering, Tohoku University, 6-6-07 Aoba, Aramaki-aza, Aoba-ku, Sendai 980-8579, Japan*

[¶]*Institute for Theoretical Physics, Center for Extreme Matter and Emergent Phenomena, Utrecht University, Princetonplein 5, 3584 CC Utrecht, The Netherlands*

E-mail: M.A.vanHuis@uu.nl; A.vanBlaaderen@uu.nl

Abstract

Yolk-shell or rattle-type particles consist of a core particle that is free to move inside a thin shell. A stable core with a fully accessible surface is of interest in fields such as catalysis and sensing. However, the stability of a charged nanoparticle core within the cavity of a charged thin shell remains largely unexplored. Liquid-cell (scanning) transmission electron microscopy (LC(S)TEM) is an ideal technique to probe the core-shell interactions at nanometer spatial resolution. Here we show by means of calculations and experiments that these interactions are highly tunable. We found that in dilute

solutions adding a monovalent salt led to stronger confinement of the core to the middle of the geometry. In deionized water the Debye length κ^{-1} becomes comparable to the shell radius R_{shell}, leading to a less steep electric potential gradient and a reduced core-shell interaction, which can be detrimental to the stability of nanorattles. For a salt concentration range of $0.5 - 250\,\text{mM}$ the repulsion was relatively long-ranged due to the concave geometry of the shell. At salt concentrations of 100 and 250 mM the core was found to move almost exclusively near the shell wall, which can be due to hydrodynamics, a secondary minimum in the interaction potential or a combination of both. The possibility of imaging nanoparticles inside shells at high spatial resolution with liquid-cell electron microscopy makes rattle particles a powerful experimental model system to learn about nanoparticle interactions. Additionally, our results highlight the possibilities for manipulating the interactions between core and shell that could be used in future applications.

Keywords

rattle particles, yolk-shell, nanoparticles, liquid-cell electron microscopy, electrical double layer, electrostatic interactions

Rattle-type or yolk-shell particles are particles where a core is enclosed by a hollow and often porous shell, via a core@void@shell structure.[1–6] When dispersed in a liquid, in our case water, the liquid can enter the porous shell to form a core@water@shell structure with a mobile core particle. The small core particles are often metal or metal oxide nanoparticles with specific catalytic,[5,7] optical[8,9] or magnetic[10] properties. Small ions and molecules can travel through the porous shell, which allows them to interact with the core particle inside. Rattle-type particles are promising for application in catalysis,[5,11–16] biomedicine,[17,18]

drug delivery,[19,20] sensing,[21–25] adsorbents,[26,27] lithium-ion batteries,[28] optical devices,[8,9] and many other applications. These may require the particle to move freely, e.g. to maximize accessible surface area, which makes studying the stability of the particle within the shell relevant.

Liquid-cell electron microscopy (EM) is capable of *in situ* imaging of particles at nanometer resolution.[29–31] We recently observed that Brownian motion is unaffected by the electron beam at low enough electron dose rates,[32] which was reported recently also by Yesibolati and coworkers.[33] As water is an important medium for both biological and synthetic systems and their applications, we decided to use it as a medium in this work. However, nanoscale and sub-micron sized objects in water move too fast to be tracked for most EM imaging systems. Due to the confining nature of the geometry, the particle is unable to leave the shell and can therefore be imaged, even though it diffuses rapidly. In water, the relevant interactions for nanoscale objects are effective at a length scale of nanometers to hundreds of nanometers. Therefore, any technique used to investigate the interaction potential of such objects needs to have nanometer spatial resolution. Other studies have shown that it is possible to infer an interaction potential from observations made with liquid-cell electron microscopy, even if those particles were trapped near the surface of the liquid-cell geometry.[34,35] Additionally, the flow-through capability of the liquid-cell holder allows control over essential solution parameters such as pH and ionic strength *in situ* and makes it possible to observe direct changes in the interaction potential and the colloidal stability of the core particle within a shell, when the shell is adsorbed to one of the windows of the liquid-cell.

The interactions between spherical charged colloidal particles dispersed in a liquid is an extremely well-studied topic within colloid science[36–63] and here is certainly not the place to review this topic in any depth.[39–46] Understanding the interactions between colloidal particles is not only of importance to almost all applications in which colloids are used, but has over the last century also become an important topic in 'multiple-particle' statistical physics where one of the goals is to derive effective potentials from a lower level description.[39–46] The

description of the interactions between charged spheres that is most often used in theoretical and experimental studies is referred to as the DLVO potential. DLVO refers to Derjaguin, Landau, Verwey and Overbeek, who were the principle investigators that developed the theoretical framework to describe these interactions, mostly in the forties of the previous century.[36–40] It may come as a surprise that the strongly related topics of the dynamics and interactions of a spherical particle that is present inside a liquid-filled spherical shell are much less well studied[64,65] despite the already mentioned recent progress in realizing such systems. This lack of knowledge is for instance illustrated by a recent paper in which is the first to theoretically describe the dynamics of a single charged colloidal particle in between two flat, confining walls where the range of the double layer repulsion and the distances between the walls are similar.[47] It should additionally be remarked that this flat-plate geometry of the confinement is significantly simpler than that of a spherical particle inside a spherical shell.[47,48] The reason for the absence of theoretical studies is almost certainly due to a lack of experimental studies in which accurate local dynamics and/or interaction potentials under similar confining geometries have been measured. There is also a strong need for experimental studies on the more-or-less direct measurements of colloid-colloid interaction potentials for nanoparticles (NPs). The reason for the lack of studies is, besides the necessarily higher spatial resolution needed and much smaller volume of the NPs, additional experimental difficulties. For example, optical tweezers cannot be used to measure NP interactions,[51] but have been used frequently for larger sized colloids.[52,53] Additionally, there is also the much higher diffusion coefficient of nanoparticles. These factors combined mean that besides the already mentioned liquid-cell TEM studies, that were performed on nanoparticles close to a surface,[34,35] we are aware of only a handful of other studies in which NP interactions were more-or-less determined directly,[66] e.g. by cryo TEM studies.[49,50] However, even in these studies[49,50] the NPs were either adsorbed onto a liquid interface or close to such an interface which most likely strongly affects the inter particle potentials. Work is under way,[50] also in our group, to try to extend this cryo-TEM methodology to measure the radial distribution

functions for 3D NPs systems. However, as mentioned, at present, interaction potentials of 3D systems have only been measured for much larger colloidal particle systems.[42,52–55] An incomplete set of examples and techniques for such interaction potential measurements is: direct imaging in 3D,[55] optical tweezers[51–53] and atomic force microscopy.[55]

Interesting phenomena arise for conditions where the Debye-Hückel screening length κ^{-1} is larger or similar to the average distance between particles.[48,53,54,56–63] It was already realized by Overbeek and Albers[57,58] when they studied the colloidal stability of micron-sized water emulsion droplets in apolar solvents, that for such systems the screening length could achieve much larger values (several μm) as opposed to values that can be obtained in water by deionization (several hundred nm at most) because of the self-dissociation of water. When κ^{-1} becomes larger than the distance between the particles, complete double-layer overlap cannot occur and particles start to experience significant interactions from second shell neighboring particles. Additionally the potentials can become non-additive.[62] These combined effects average out repulsions and diminish the stability of these particles when compared to (much) lower volume fraction conditions.[57,58] It is even possible that the pair potentials under extreme low salt conditions can become more Coulomb-like, rather than follow the Yukawa interaction potential that describes screened charges[60] and/or that counter ion condensation takes place (a non-linear screening effect).[61] The only reason that such drastic effects have not yet been reported for nanoparticles in water is related to the difficulty of measuring potentials between nanoparticles.

However, this phenomenon can be studied for nanoparticles inside spherical shells filled with water mostly because of the particular geometry and (much) smaller distances involved compared to κ^{-1}. Under these conditions, the counterions of the charged particles cannot be neglected w.r.t. the concentration of the background ionic strength and the definition of κ^{-1} becomes more ambiguous.[60] Additionally, there are specific issues that are related to the geometry of a shell that is porous to ions. Because of the procedures in which (our) particles with a movable core inside a shell are made, the spherical shells are often

(meso)porous. The reason for this is that the liquid-filled shells are often made hollow by either an etching process or a burning away of an interior organic layer. This means that sufficiently small ions can move through the shell from the outside liquid to the inside and vice versa. However, the speed with which ion transport through the shell occurs w.r.t. the dynamics of the moving core particles is usually significantly lower than that of the ions freely diffusing in the liquid, thus possibly undermining certain assumptions made in the theoretical description. The dynamics of the ions going through the shells is not characterized in the present work as well and is left for future work. Additionally, even without the charge-induced interactions, a diffusing particle inside a hollow shell already has a complex position-dependent mobility because of the boundary conditions of the hydrodynamics.[47,48,64,65] The coupling between the interactions and the hydrodynamics only complicates this further.[47] However, this involved position dependence also holds promise, as it can be used to locally measure the temperature and/or ionic strength if the dynamics of the ions and interactions with the shells are sufficiently well understood theoretically and controlled experimentally. Moreover, it is clear from the above that this geometry as it already can be studied in a liquid-cell by high resolution imaging is also a powerful experimental model system to learn about interactions of nanoparticles in 3D in different solvents, including water for the first time in experiments.

Results & Discussion

In this study, we imaged rattle-type particles in water while changing the salt concentration *in situ*. We investigated two kinds of rattle-type particles (Figure 1). The first kind are composed of a submicrometer-sized titania core and a silica shell (Figure 1a), which were made by removing a polystyrene sacrificial layer by calcination.[9] They are promising building blocks for novel optical colloidal crystals, because the locations of cores in the shell compartment can be reversibly controlled using external stimuli.[9] The second kind are nanorattles

consisting of a gold nanoparticle in a silica shell (Figure 1b), which were synthesized by a surface-protected etching process[67] that removes a sacrificial silica layer and are promising materials for sensing.[25] The diameter of the core, inner diameter of the shell and the thickness of the shell, as well as the zeta potential of the core particle, are reported in Table 1. Details of the synthesis procedure can be found in the Supporting Information and previous work by Watanabe and coworkers.[9,25]

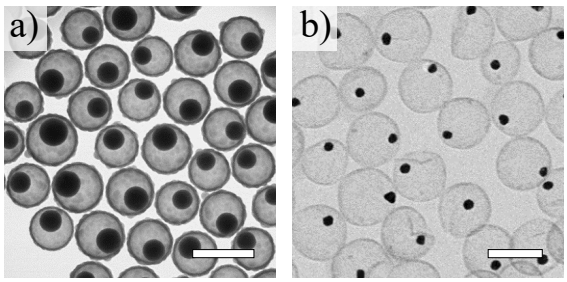

Figure 1: Rattle-type particles used in this study imaged with TEM in vacuum. a) Titania@void@silica rattles. The scalebar represents 1 micron. b) Gold@void@silica rattles. The scalebar represents 250 nm.

Table 1: Measured quantities of the two types of rattles used in this work: core radius R_{core}, inner shell radius $R_{\text{shell,inner}}$, shell thickness T_{shell} and zeta potential of the core ζ_{core}. The zeta potential of the core particle was measured in aqueous solution at a pH of 7 and an ionic strength of 1.00 mM LiCl salt.

Particle	R_{core} **(nm)**	$R_{\text{shell,inner}}$ **(nm)**	T_{shell} **(nm)**	ζ_{core} **(mV)**
Titania@void@silica	165 ± 18	357 ± 24	27 ± 2	-54 ± 1
Gold@void@silica	17 ± 2	86 ± 5	5 ± 1	-50 ± 4

In short, the rattle-type particles were investigated using liquid-cell scanning transmission electron microscopy (LC-STEM). The dispersion of rattles in water was dropcast onto a glow-discharged Si microchip in a dedicated holder and a second Si microchip was placed on the bottom chip. The closed holder was introduced into the microscope and deionized water was flowed through the liquid-cell at a rate of $2\,\mu$l/min for 45 min. The flow was turned off for imaging of the moving core particle inside a shell that was attached to the electron-transparent window of the liquid-cell. Subsequently, a new LiCl concentration was flowed into the shell at a rate of $2\,\mu$l/min for 15 min. The moving core particle was then imaged

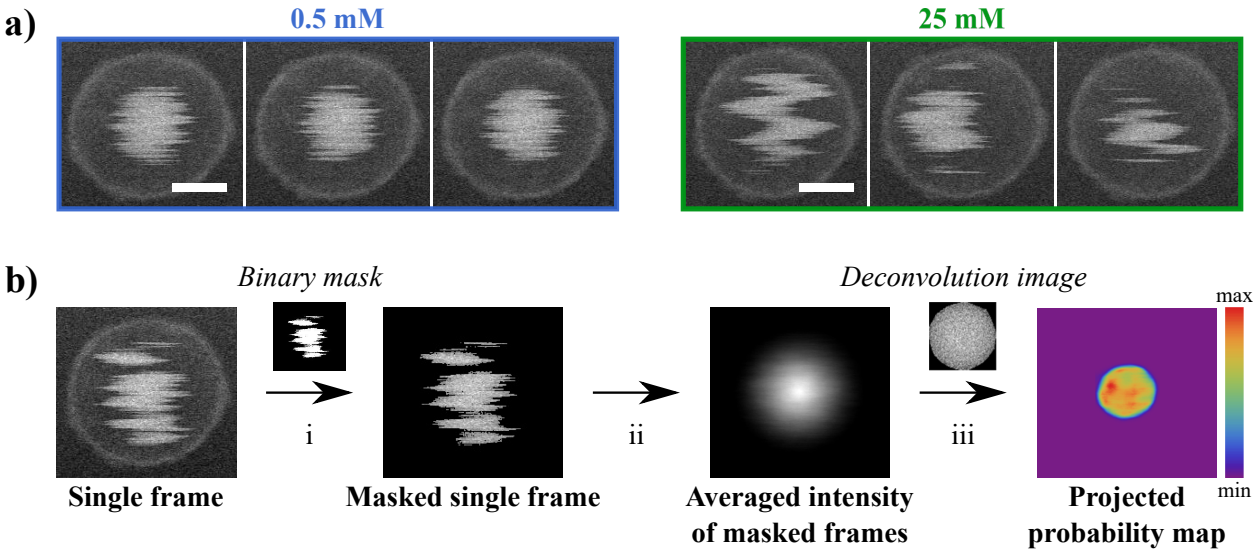

Figure 2: Experimental data and analysis. a) Typical images of a moving titania particle in a shell in 0.500 and 25.0 mM LiCl in water. The frame time was 1 s and the electron dose rate was 45 $e^{-}nm^{-2}s^{-1}$. The scalebars indicate 250 nm. b) Procedure to analyze the data in order to extract the probability of finding the particle at certain positions within the shell. i) For each single frame a binary mask was made that detects the signal of the particle. This mask was used to make a masked single frame that is black everywhere, but had the original intensity of the pixels where the particle was. ii) All masked single frames were averaged to obtain an averaged intensity of the moving core particle. iii) The averaged intensity was corrected for the available volume in the z direction (Supporting Information) and deconvoluted with a modelled image of a titania particle of the same size. This resulted in a projected probability map of where the particle can be found within the projected shell.

again with the flow turned off. This procedure was repeated for all salt concentrations. Typical resulting images for the titania@water@silica rattles in 0.500 and 25.0 mM LiCl (aq) with a frame time of 1 s are shown in Figure 2a. Due to the high mobility of the core particle in water the particle could not be tracked directly. Using the analysis outlined in Figure 2b a measure of the probability of finding the particle at certain positions within the shell was obtained. We filtered the intensity from the core particle of every single frame and averaged those in a single image. We then corrected for the available volume in the z direction (Supporting Information) and deconvoluted with a simulated image of a titania particle to obtain a projected probability map of finding the particle in a certain position within the projected shell. Details of the data acquisition and image simulation and processing are given in the Methods Section.

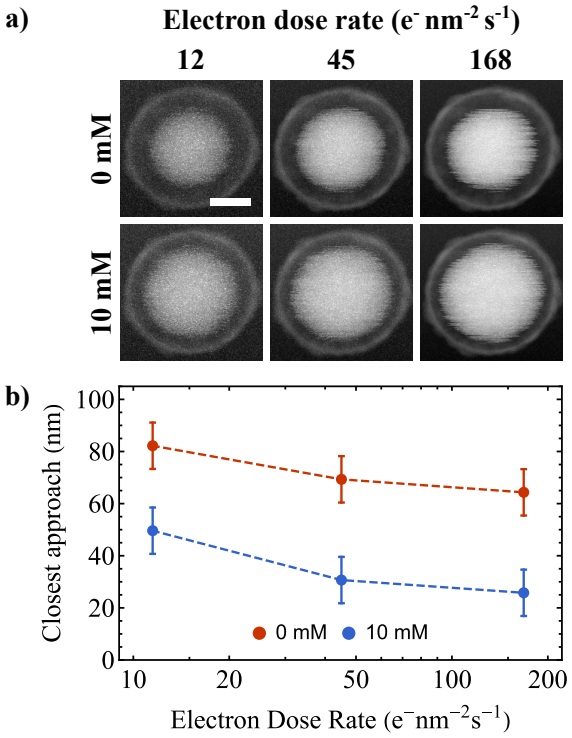

Figure 3: Influence of the electron dose rate on the repulsive interaction within a titania@water@silica rattle-type particle. a) The 6 images show the maximum intensity for each pixel that was reached during the whole image series at a certain electron dose rate. This visualizes what the minimum distance of approach is between the core particle and the shell. The scale bar is 250 nm. All images were taken at the same magnification. b) The minimum distance decreases with the electron dose rate for deionized water and 10.0 mM LiCl in a similar way.

Before results can be interpreted, as in any experiment involving liquid-cell electron microscopy, the influence of the electron beam has to be investigated.[68] Figure 3 shows images of the maximum intensity of all pixels throughout the whole image series for a titania core exploring a silica shell. This effectively visualizes how close the core particle was able to approach the shell throughout the complete image series. It is evident that the core particle approached the shell more closely at higher electron dose rates. This means that the electron beam influenced the interactions between the titania particle and the silica shell. Earlier studies have observed changes in the interactions between NPs in LC-STEM and argued they could be caused by either a change in pH[69] or a change in the ionic strength.[34] A significant change in the local temperature is not expected at these electron dose rates.[70]

We used different electron dose rates to investigate titania@water@silica rattle particles in deionized water and in 10.0 mM LiCl in order to distinguish between the pH or the ionic strength being influenced by the electron beam irradiation. We observed that a similar decrease in minimum distance of approach to the shell for increasing electron dose rates occured in deionized water and 10.0 mM LiCl (Figure 3). From this we infer that the change in ionic strength is not the main contributing factor in our system. We believe the change in the core-shell interaction can be explained by taking into account a change in pH due to electron-water interactions. As more H_3O^+ than OH^- is produced, the pH drops when water is irradiated with the electron beam.[69] It is well known that both titania and silica lose charge when the pH drops.[71–73] Additional experiments on how the influence of the electron beam seems related to pH can be found in the Supporting Information. We performed our experiments for titania@water@silica rattles at a moderate dose rate of $45\,e^-nm^{-2}s^{-1}$ to overcome the change of interaction at high dose rate, while obtaining an acceptable signal-to-noise ratio. For this dose rate, the decrease in range of the repulsive interactions due to the electron beam is likely to be only a few nanometers, while the range of interactions for which we extract interaction potentials in this work is $15 - 100$ nm.

Interactions within a titania@water@silica rattle-type particle

Having determined the influence of the electron beam, we next aimed to investigate the influence of the ionic strength on the interaction potential between a titania core and a silica shell (Supporting Movie S6). The salt we used was LiCl, as these (solvated) ions most likely diffuse through the porous silica shells.[74] Figure 4 shows the influence of the salt concentration on the projected probability of finding the titania particle in a certain position within the shell. In Figure 4a the projected probability maps for all salt concentrations are given for a single rattle-type particle. Figure 4b and 4c show the projected probability as a function of the projected core-to-shell distance. The projected probability for a particle in low salt concentrations in Figure 4b was fitted to a 3D interaction potential, resulting in

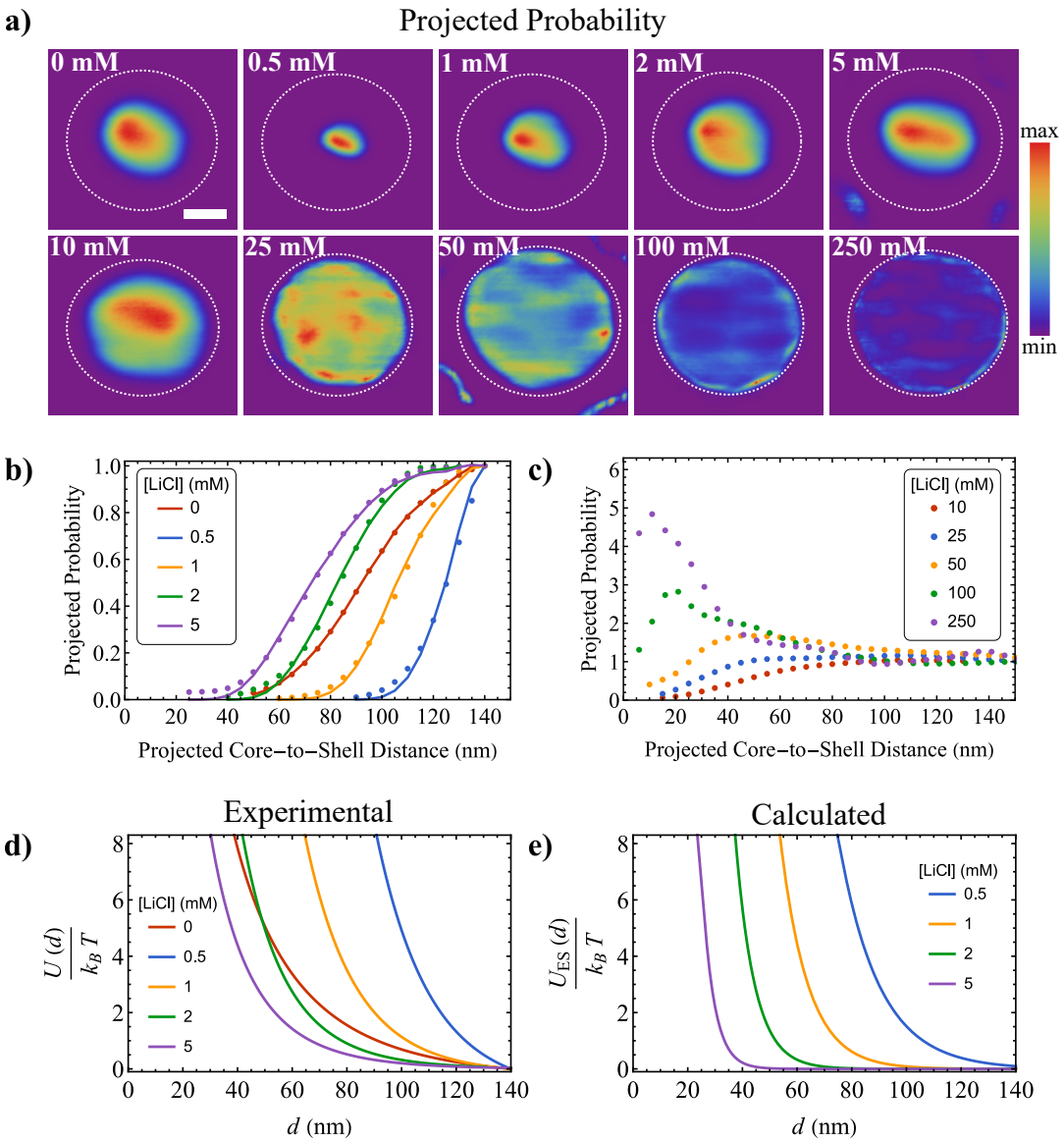

Figure 4: Influence of the salt concentration on the interactions between the titania core and the silica shell in a titania@water@silica rattle-type particle. a) Projected probability maps of finding the core particle in a certain part of the projected shell. The dashed circles show the projected area available to the particle in the shell. The scalebar indicates 100 nm. b-c) Projected probabilities of finding the particle a projected distance away from the shell wall at various salt concentrations. The projected probabilities for each concentration were averaged over 3 different particles. d) 3D interaction potentials obtained from the fits in b. e) Electrostatic interaction potentials calculated by solving the non-linear Poisson-Boltzmann equations with constant surface potential using a finite-element method for a core particle with radius $R_{\text{core}} = 170\,\text{nm}$ and surface potential $\psi_{\text{core}} = -50\,\text{mV}$ inside a shell with inner radius $R_{\text{shell}} = 350\,\text{nm}$ and inner surface potential $\psi_{\text{shell}} = -60\,\text{mV}$.

Figure 4d. In short, we assumed a perfectly spherical rattle geometry and used the relation between the interaction potential $U(r)$ and probability $P(r)$ to find a particle at a certain radial position

$$\frac{U(r)}{k_B T} = -\ln\left(P(r)\right). \tag{1}$$

Projecting a probability derived from a trial potential $U_{\text{trial}} = A\frac{e^{-\kappa r}}{r}$, with κ (the inverse Debye length) and A as fitting parameters, and fitting this to the experimental projected probability of finding the core at a certain radial position allowed us to find a 3D experimental interaction potential, which is eventually expressed as a function of particle-shell distance d. Additional details can be found in the Methods Section. This fitting procedure was not performed for the projected probability for a particle in high salt concentrations in Figure 4c, as the origin of the high projected probability close to the projected shell is uncertain, as will be discussed later. Finally, Figure 4e shows the results of finite-element calculations for a rattle geometry solving the non-linearized Poisson-Boltzmann equation for a symmetric 1:1 electrolyte:

$$-\epsilon_0 \epsilon_r \nabla^2 \psi = 2 c_0 \text{sinh}\left(\frac{e\psi}{k_B T}\right). \tag{2}$$

Here ψ is the electric potential, ϵ_0 is the permittivity of vacuum, ϵ_r is the dielectric constant of the liquid, c_0 is the salt concentration, e is the electron charge, k_B is the Boltzmann constant and T is the temperature. On the surface of the core and the shell we assumed constant surface potential boundary conditions. Three interesting points arise from Figure 4. First, the electrostatic repulsion had a longer range than expected for sphere-sphere interactions. Second, when no salt is added the titania particle approached the shell more closely than when 0.500 or 1.00 mM LiCl was added, even though the Debye screening length is significantly longer in deionized water. Third, the titania particle remained colloidally stable within the shell up to 250 mM LiCl and was found to be more often close to the shell than in the middle of the geometry. We discuss these three phenomena in the following sections.

First, let us turn to the long-ranged electrostatic interaction between a sphere and a

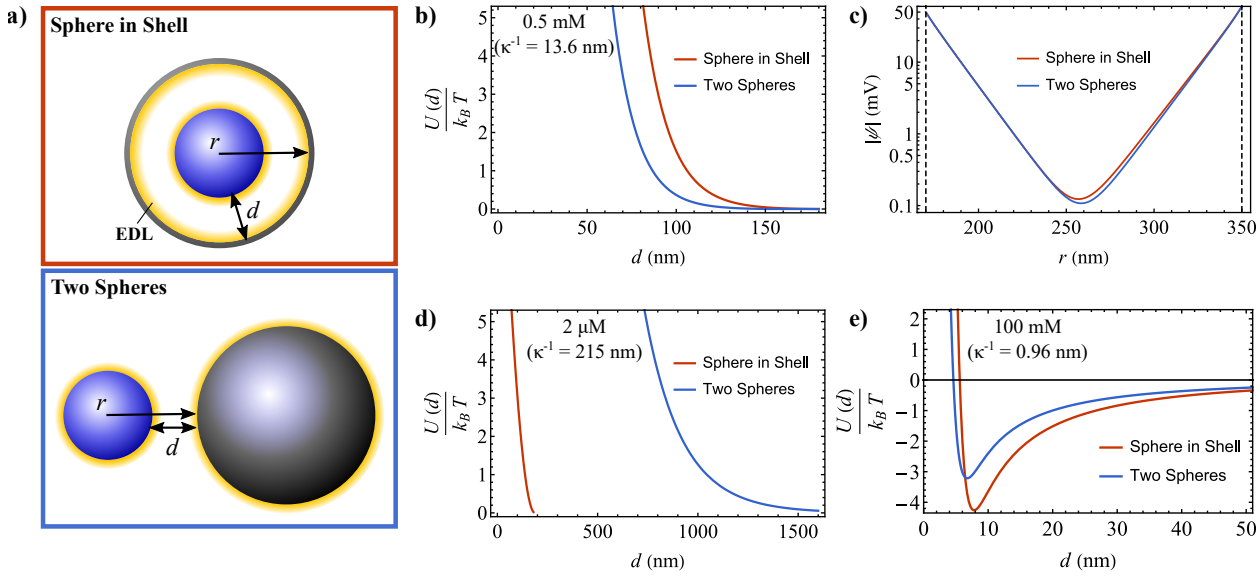

Figure 5: Comparison of the calculated interaction between two spheres and a sphere and a shell. One sphere has the radius (170 nm) and surface potential (−50 mV) of the core particle, while the other sphere has the radius (350 nm) and surface potential (−60 mV) of the inner shell wall. a) The two geometries used for the calculations. b) The interaction potential $U(d)$ for a sphere in a shell compared to two spheres for an ionic strength of 0.5 mM. c) The electric potential ψ as a function of the radial coordinate for the same conditions as in b. The left-hand side of the plot shows the decay of the surface potential from the core particle/small sphere, while the right-hand side of the plot shows the decay of the surface potential from the inner shell wall/large sphere. d-e) The interaction potentials for sphere-sphere and sphere-shell systems for ionic strengths of 2 μM and 100 mM, respectively. Van der Waals interactions of a sphere within a shell have been included in e.

shell. The experimental interaction potentials are less steep than the calculated potentials, which is likely due to experimental limitations such as resolution. Using the equations outlined in the work of de Jonge[31] we estimate the resolution in our experimental data to be approximately 11.6 nm in our experiments with titania@water@silica rattle-type particles (Supporting Information). Errors in the determination of the interactions between the core and shell mostly stem from resolution and the 2D projection of a 3D system. The resolution likely leads to errors in determining the projected core-shell distance and less steep interaction potentials. The 2D projected data leads to a lower accuracy of the projected probability when the particle is near the projected shell wall. Despite the errors in the experimental data it shows the same trends as the calculations and the long-ranged character of the interaction

potential is present for both the experiments and the calculations. To get more insight in this long-ranged repulsion, we calculated the electrostatic interaction for both a sphere-sphere system and a sphere-shell system using a finite-element method to solve the non-linear Poisson-Boltzmann equation with constant surface potential boundary conditions. The result for various salt concentrations is shown in Figure 5. For the case of an ionic strength of 0.5 mM in Figure 5b, it is indeed observed that the interaction is longer ranged for a sphere in a shell compared to the interaction between two spheres. The distance d between the two surfaces for which the repulsion is $5\,k_BT$ is approximately 65 nm for sphere-sphere interaction, while it is approximately 82 nm for sphere-shell interaction. This difference is more than one Debye length (for 0.5 mM, $\kappa^{-1} = 13.6$ nm), which is quite significant. In Figure 5c it is shown that the potential from the surface of the inner shell wall (right-hand side of the plot) decays more slowly than that of a spherical particle; the difference is more pronounced when the core is off center (Supporting Information). This is due to the concave geometry of the shell as found previously for hollow shells.[75] This slow decay of the electric potential is the reason for the long-ranged interaction in a sphere-shell system. Furthermore, it is likely a reason why the core particle was stable at 250 mM concentration of LiCl.

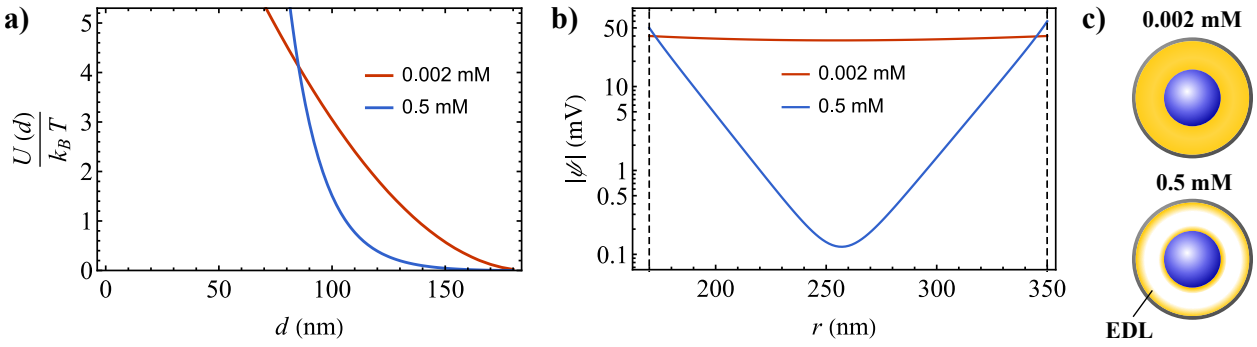

Figure 6: Calculated electrostatic interactions for a particle in a shell for an ionic strength of 2 μM ($\psi_{\text{core}} = -40$ mV and $\psi_{\text{shell}} = -40$ mV) and an ionic strength of 0.5 mM ($\psi_{\text{core}} = -50$ mV and $\psi_{\text{shell}} = -60$ mV). a) The interaction potential. b) The electric potential decaying from the core particle surface (left-hand side) and the inner shell surface (right-hand side). c) Schematic representation of the electric double layers within the rattle geometry.

Second, the apparently weak core-shell interaction in deionized water was investigated. In Figure 4b and 4d it is shown that the core particle is less confined to the middle of

the shell for deionized water compared to moderate amounts of salt in the solution (0.500 and 1.00 mM LiCl, respectively). Furthermore, the interaction potential in deionized water was less steep than those in moderate amounts of salt. In Figure 5d we observe that the interaction in deionized water (we assume an ionic strength of $2\,\mu$M) for two spheres is in the range of the order of a micron. This range is much larger than the space available in the rattle geometry. As such complete double layer overlap cannot occur, the interaction between core and shell is significantly altered. Figure 6 explores this in more detail by comparing the calculated core-shell interaction in deionized water (ionic strength of $2\,\mu$M, $\kappa^{-1} = 215\,$nm) with the interaction for an ionic strength of 0.5 mM ($\kappa^{-1} = 13.6\,$nm). The interaction in $2\,\mu$M salt is significantly less steep than the interaction in 0.5 mM salt. Figure 6b shows that when the core particle is in the middle of the shell, the electric potential ψ originating from the surfaces of the core and the shell decays to almost 0 in the middle between the two surfaces. However in deionized water, the electric potentials coming from both the surface of the core particle and the inner shell surface hardly decay. This leads to an almost flat electric potential within the entire shell geometry, significantly reducing the electrostatic interaction between core and shell. It is remarkable that this phenomenon was found in water. As previously stated, due to the self-dissociation of water it is difficult to reach ionic strengths lower than $1\,\mu$M and Debye lengths larger than 300 nm. The shell geometry helps significantly in this regard. The core particle cannot escape the shell and can only be a maximum distance away from the shell wall at all times. Furthermore, the slower decay of the electric potential from the inner shell surface means the electric potential is even more flat due to the rattle geometry.

Third, we discuss the interesting phenomenon at high ionic strength for which the core particle spends more time near the projected shell than in the middle of the rattle geometry (Figure 4c). One explanation is the presence of an attractive potential that the core experiences when it is close to the shell. The likelihood of van der Waals attractions are a good candidate for such attractions according to the calculations (Methods Section) and

as shown in Figure 5e, where the sphere-shell secondary minimum is more severe than the sphere-sphere secondary minimum. However, in our sphere-shell system, there was also an influence of hydrodynamic interactions when the core particle was near the shell wall. This slowed down the particle near the shell wall, similarly to how it would near a flat surface.[47,76]

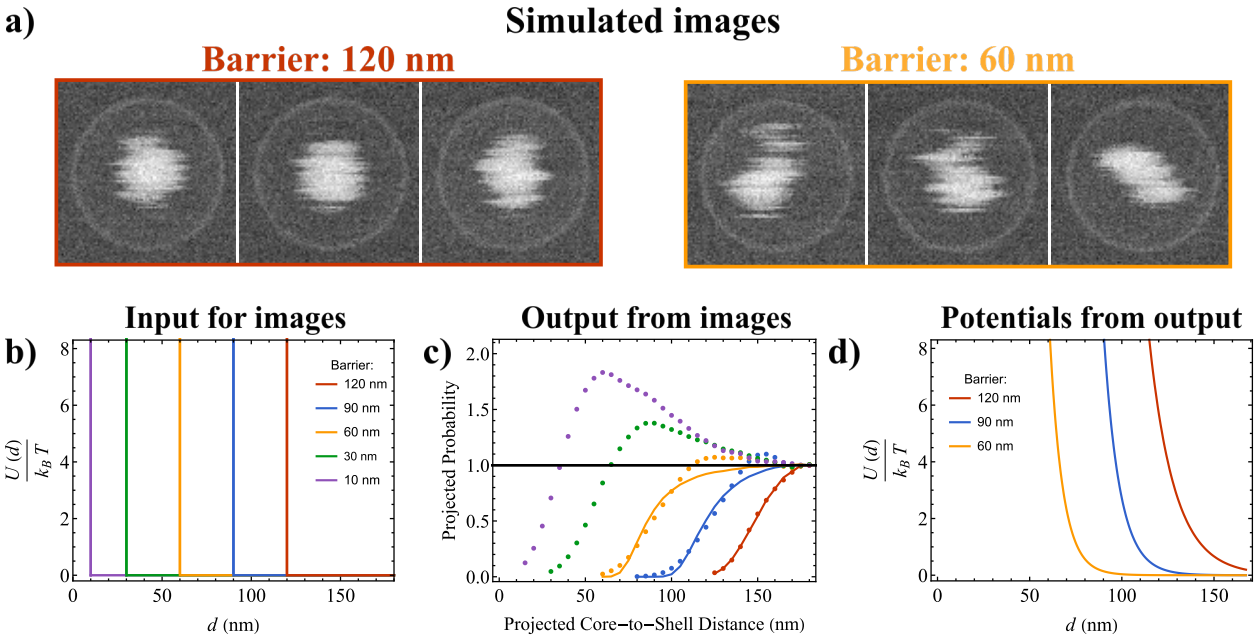

Figure 7: Results obtained by simulating ADF-STEM images of a moving titania core particle ($R_{\text{core}} = 170\,\text{nm}$) within a silica shell ($R_{\text{shell}} = 350\,\text{nm}$) in water. a) Example images of a moving core particle that cannot approach the shell wall closer than 120 or 60 nm. b) The input interaction potentials used to simulate the diffusion of a core particle within a shell. c) Projected probability as function of the projected core-to-shell distance for the various simulations performed with potentials shown in b as barriers. d) The resulting apparent interaction potentials found from the projected probability fits in c for the three cases where the particle was confined mostly to the middle.

Therefore, we investigated how hydrodynamic slowing down of the core particle shows up in the analysis of our experimental microscopy data due to the finite time of our measurements. We are aware of the fact that in equilibrium statistical mechanics the effects of hydrodynamics cannot be part of a probability (density). However, because of the finite time of our measurements, hydrodynamic effects can and do show up. As these effects are not correctly taken into account, the probability function should then more correctly be labeled as 'apparent probability density'. To uncover how much hydrodynamic interactions influ-

enced our experimental data, we simulated ADF-STEM images of a core particle diffusing within a shell. In short, for every timestep (equal to the pixel dwell time) we let the particle (starting from a random position within the shell) move in a random direction according to the position-dependent and direction-dependent diffusion coefficient (Figure S5a). Knowing the position of the particle for the pixel that is currently being scanned, we took the weighted average value of that pixel for the three static simulated images of the rattle particle for which the position of the core particle best resembled the current position. This was done for all pixels in order to form an image of a moving core particle within a shell. We simulated 180 images per series, which is roughly the same amount as the images per salt concentration in the experiments. More details can be found in the Methods Section. Figure 7a shows images resulting from this simulation for which the particle could move freely until it approached 120 or 60 nm from the shell wall, respectively (Figure 7b). The simulated images look similar to the experimental images shown in Figure 2a. In Figure 7c the projected probabilities of finding the particle at a certain distance from the shell from simulated images are shown. We observed that when the particle was allowed to approach the shell closely, the projected probability of finding the core particle near the shell wall was higher than in the middle of the shell geometry. Since there was no attractive potential in our simulations, this was a direct consequence of the hydrodynamic slowing down of the core particle. It is thus likely that hydrodynamics effects contribute to the higher projected probability of finding the particle near the projected shell wall found in Figure 4c due to the finite time of our measurements. Both hydrodynamic effects and van der Waals attractions could lead to the increased probability of finding the core particle near the projected shell wall in our measurements. Since it was hard to distinguish between both effects (Supporting Information) we did not attempt to extract the interaction potential at high salt concentrations.

However, when the particle was not allowed to move close to the shell wall the effect of the hydrodynamics proved much more limited. Figure 7d gives a good impression of the systematic error that hydrodynamic interactions, but more importantly limited resolution,

would induce on the potentials we extracted in Figure 4d for the cases of moderate salt concentrations ($0.5 - 5\,\mathrm{mM}$). Based on the magnitude of these apparent potentials, we are confident in our extracted interaction potentials in Figure 4d.

Interactions within a gold@water@silica nanorattle

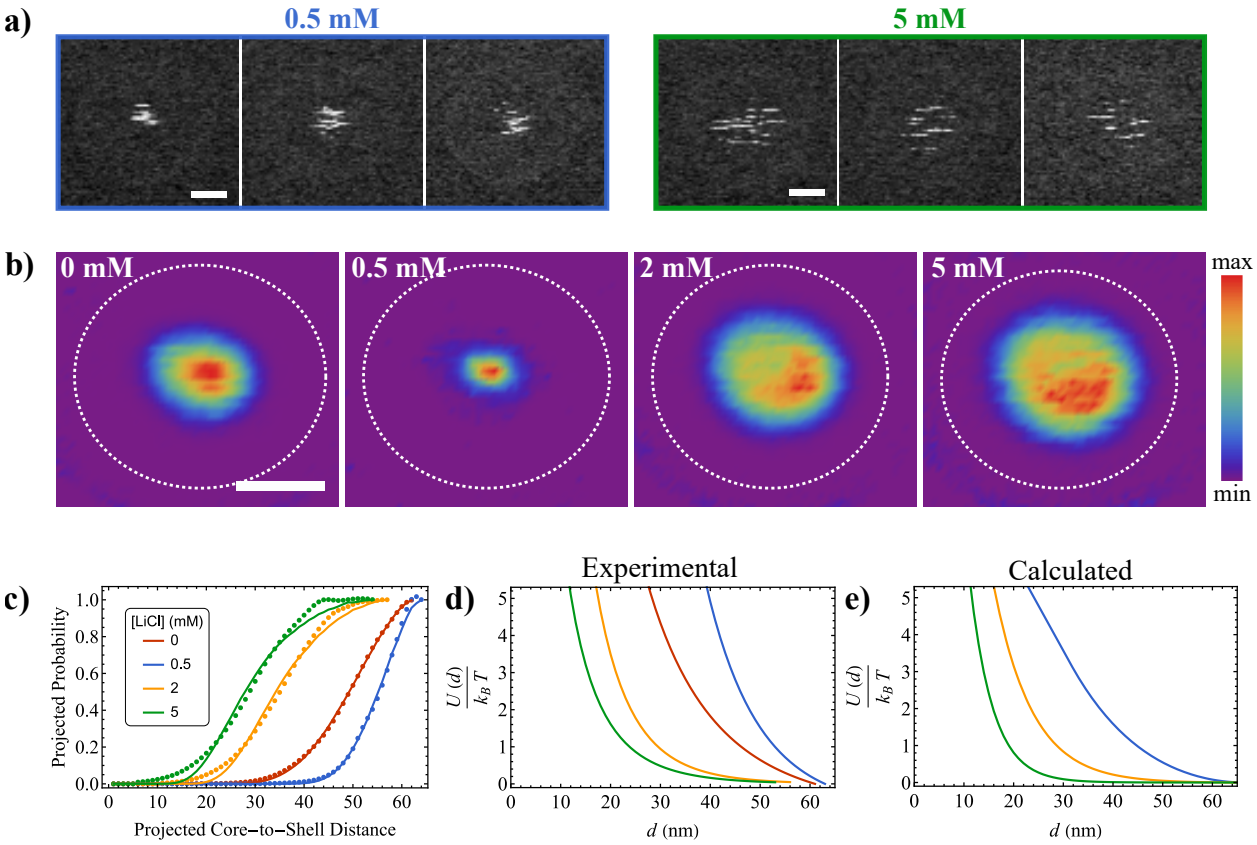

Figure 8: Interactions of a gold nanosphere ($R_{\mathrm{core}} = 17\,\mathrm{nm}$) inside a thin silica shell ($R_{\mathrm{shell}} = 80\,\mathrm{nm}$). a) Example experimental images of a gold particle moving within a silica shell in water with 0.500 or 5.00 mM LiCl. The electron dose rate was $206\,\mathrm{e^{-}nm^{-2}s^{-1}}$. b) Projected probability maps of where the gold particle is found in different salt concentrations for a single particle. The dashed circles show the projected area available to the particle in the shell. c) Projected probability as function of the projected core-to-shell distance including fits for a 3D interaction potential. d) 3D experimental interaction potential following from the fits in c. e) Calculated interaction potential by solving the non-linear Poisson-Boltzmann equation for a gold particle ($\psi_{\mathrm{core}} = -50\,\mathrm{mV}$) within a silica shell ($\psi_{\mathrm{core}} = -60\,\mathrm{mV}$) with constant surface potential; we omit the 0 mM result as it is a problematic limit. All scalebars indicate 50 nm.

Lastly, the interactions between a gold nanosphere ($R_{\mathrm{core}} = 17\,\mathrm{nm}$) and a thin silica shell

($R_{\mathrm{shell}} = 80\,\mathrm{nm}$) were investigated in Figure 8. These particles can really be considered nanorattles and are so small that liquid-cell electron microscopy is the only technique that is able to obtain reliable real space information on them in water as a solvent. The electron dose rate in these measurements was $206\,\mathrm{e^-nm^{-2}s^{-1}}$. As found for the titania particle, the experimental interaction potentials are not as steep as the calculated potentials. However, this effect is less pronounced as the resolution is slightly better imaging gold particles (7.8 nm) compared to titania cores (11.6 nm). Especially the calculated and experimental interaction potentials for 2.00 and 5.00 mM LiCl agree excellently. Interestingly, the experimental potential for an ionic strength of 0.500 mM indicates a repulsion of longer range than the calculated interaction potential. This could be due to an underestimation of the surface potential in the calculations. For gold@water@silica rattles, similarly to the much larger titania@water@silica rattles, the core particle approached the shell more closely without any added salt, compared to the situation for 0.500 mM LiCl. Moreover, we observed many instances of the gold core particle getting stuck to the shell in pure water (Figure S12 and Movie S8). There are even instances where the particle got stuck to the shell in one frame and the electron beam enables it to move again the next frame. The influence of the electron beam is hard to determine here, but the particle getting stuck to the shell only happens when no salt was added, which hints that the repulsion between the core and shell was lowest for this case. These results indicate that in these nanorattles flat electric potentials can be detrimental to the stability of the core particle within the shell, especially when the surfaces are not highly charged or when they are in a medium with a less polar character than that of water. It is therefore recommended to have some salt present in dispersions of nanorattles at all times if mobility of the core particle is desired.

Conclusion

In conclusion, it was found that it is possible to measure reliable interactions between a core particle and a shell using liquid-cell electron microscopy. We found that the interactions between a titania core and silica shell could be tuned over a large range of ionic strengths. The interactions of a sphere within a shell were found to be significantly more long-ranged compared to the interactions between two spheres under the same conditions. It was also observed that the core particle could approach the shell more closely when no salt was added, compared to the case for moderate salt concentrations (0.5 and 1 mM). Finite-element calculations confirmed this to be due to a flat electric potential within the rattle geometry in deionized water. Furthermore, for salt concentrations above 50 mM, the core particle spent more time close to the shell wall than in the middle of the rattle geometry. Simulations confirmed that hydrodynamic slowing down of the core particle plays a significant role, while calculations also showed a secondary minimum in the potential of a few k_BT was probable at such high salt concentrations as well, contributing to the above mentioned behavior. Due to the limit of our 2D projected experimental data, the extent of both effects could not be determined accurately experimentally.

Lastly, the interactions between a gold nanosphere and a silica nanoshell were measured in aqueous solutions. We found that, due to the flat electric potential within the shell, the nanosphere is less stable within the shell in deionized water, compared to when a moderate amount of salt was added ($0.5 - 5$ mM). The results indicate that liquid-cell electron microscopy is a powerful tool to measure interactions of nanoparticles in water, where a high spatial resolution is a requirement.

Methods Section

Liquid-cell STEM

In order to image the rattle-type particles in the electron microscope, we used a liquid-flow TEM holder with corresponding microchips (Hummingbird Scientific, USA). The microchips support 50 nm thick amorphous silicon nitride (SiN_x) windows with lateral dimensions of 50 by 200 μm^2. A sample cell consists of two chips separated by a spacer of 250 or 1000 nm in height, depending on the size of the rattles. The two Si chips were glow-discharged for 1 min prior to the experiment in order to make their surfaces more hydrophilic. The microchip with spacer was then placed in a dedicated holder. A 1 μL droplet of the dispersion of rattle-type particles in deionized water was dropcast onto the microchip. The second microchip was placed on the bottom chip with the hydrophilic side facing the opposite chip. The excess liquid was removed with filter paper.

The liquid-cell STEM experiments were carried out using a transmission electron microscope (Tecnai-F20, Thermo-Fischer Scientific), equipped with a field emission gun, and operating at 200 kV. The semi-convergence angle of the electron probe was 10 mrad. The annular dark-field (ADF) detector was used with a camera length of 120 mm. Image series were acquired with TEM imaging & analysis software (TIA). For the experiments with titania@water@silica rattle-type particles, the beam current measured via the fluorescent screen in vacuum was 37 pA for all videos unless specified differently. A frame recording time of 1 s was used. The number of pixels was 512×512, which resulted in a pixel size of 4.4-8.8 nm depending on the magnification. These settings resulted in an electron dose rate of 12—45 $e^- nm^{-2} s^{-1}$. For the experiments with gold@water@silica nanorattles, the beam current in vacuum was 85 pA. A frame time of 1 s was used. The number of pixels was 512×512 pixels, which resulted in a pixel size of 3.14 nm. This corresponded to an electron dose rate of 206 $e^- nm^{-2} s^{-1}$. The image series acquisitions were at least 180 frames long.

After the holder was inserted into the microscope and before image acquisition started,

deionized water was flowed through the cell at a rate of 2 μl/min for 45 min. At least 3 rattle-type particles in different parts of the liquid-cell were then imaged while the flow was turned off. We did not observe any influence of the flow on the particle mobility within the shell, but were concerned about mechanical vibrations and thus left the flow off during measurements. The shell of the rattle-type particle was stuck to the top chip of the liquid-cell and therefore only the core particle inside could move. Each particle was imaged separately and for 180-600 s per LiCl concentration. After image series acquisition for one LiCl concentration was completed, the next, more highly concentrated LiCl solution was flowed into the liquid-cell at a rate of 2 μL/min for at least 10 minutes. The flow was then turned off again for image series acquisition. This was repeated for all different salt concentrations for the same 3 particles. At the end of the experiment, a solution of pH 2 (10.0 mM HCl) was flowed into the cell. This made the silica shell charge-neutral[71–73] and the core particle irreversibly attached to the shell (Figure S10). This allowed us to measure the size of the core particle for that particular rattle-type particle.

Image processing

We used ImageJ (1.51a) and Mathematica (Wolfram, v12.2) to analyze the recordings. We used ImageJ to binarize the individual frames of the videos. These binarized images were then used as a mask to remove the background of the original images. This leaves us with the original intensity of the pixels where the particle was and black everywhere else. We then averaged all those frames into a single image. This average image was then deconvoluted with an image of a titania particle with radius $R_{\mathrm{core}} = 170$ nm as calculated with CASINO (Version 3.3.0.4, see the section on simulating static ADF-STEM images). For this we used a Richardson-Lucy deconvolution algorithm in Mathematica.[77,78] The remaining image gave a map of the probability of finding the center of the core particle in a certain projected part of the shell, which was corrected for the volume in the plane perpendicular to the image as explained in the Supporting Information.

Reconstructing the 3D interaction potential

Our experimental LC-STEM image series are 2D projections of a 3D system. In order to compare the experimental data to calculations, we need to reconstruct the effect of a 3D interaction potential between the core particle and the shell caused by the 2D projection. As the core particle is moving around randomly via Brownian motion, the probability $P(r)$ can be translated to a interaction potential $U(r)$ via

$$\frac{U(r)}{k_B T} = -\ln\left(P(r)\right). \tag{3}$$

Here r is the radial spherical coordinate. However, since the probability from our experiments is a 3D probability projected on a 2D plane, a 3D potential needs to be projected on a 2D plane, while correcting for the spherical geometry in the third dimension (Supporting Information). We do this by translating a trial potential

$$U_{\text{trial}} = A\frac{\mathrm{e}^{-\kappa r}}{r} \tag{4}$$

into a projected probability. Here κ and A are fit parameters. The fit parameters for which the projected probability distribution matches the experimental data most accurately, are assumed to be the parameters in the 3D interaction potential in our experiments.

To translate the trial potential to a projected probability we make a list of available z_i coordinates per cylindrical coordinate ρ, where the maximum z coordinate at projected radial coordinate ρ is given by

$$z_{\text{max}} = \sqrt{(R_{\text{shell}} - R_{\text{core}})^2 - \rho^2}. \tag{5}$$

Then we make a list of all the available 3D radial coordinates r_i within the cylindrical coordinate ρ:

$$r_i = \sqrt{\rho^2 + z_i^2}. \tag{6}$$

The projected probability $P(\rho)$ is then calculated by averaging all 3D probabilities $P(r)$ that fall into the projected radial coordinates ρ via

$$P(\rho) = \langle P(r_{1,2,..,n}) \rangle = \langle e^{-U(r_{1,2,..,n})/k_B T} \rangle \tag{7}$$

In the final result the interaction potential is expressed as function of the core-shell separation distance $d = (R_{\text{shell}} - R_{\text{core}}) - r$.

Interaction potential calculations

Electrostatic interaction

We performed finite element calculations using COMSOL Multiphysics (V5.4). The rattle geometry was used in an axisymmetric calculation. We solved the nonlinear Poisson-Boltzmann equation for a symmetric 1:1 electrolyte:

$$-\epsilon_0 \epsilon_r \nabla^2 \psi = 2 c_0 \text{sinh}\left(\frac{e\psi}{k_B T}\right). \tag{8}$$

Here ψ is the electric potential, ϵ_0 is the permittivity of vacuum, ϵ_r is the dielectric constant of the liquid, c_0 is the monovalent salt concentration, e is the electron charge, k_B is the Boltzmann constant and T is the temperature. On the surface of the core and the shell we put constant surface potential boundary conditions.

We exploited the rotational symmetry of the system to minimize the number of elements required. Due to the large slopes in ion concentration near the charged surfaces, a fine mapped mesh was applied from the boundary of the charged surface to a distance of one or two Debye lengths.[79,80] The Debye lengths for the salt concentrations under investigation, ranging from 0.5 to 250 mM, were between 15 nm and 0.5 nm. The mapped mesh was designed to be small near the surface and to expand radially outward. The rest of the geometry was given a free triangular mesh (Supporting Information).

We placed the core at different distances from the shell wall and solved the non-linear Poisson-Boltzmann equation. We solved for the electrostatic force on the core particle by integrating the electric Maxwell stress tensor $\mathbf{T}$ over the surface of the sphere S

$$F = \oint_S \mathbf{T} dS. \tag{9}$$

Since we required the force in the z direction, this becomes $\mathbf{T} \cdot \hat{z} = F_r \hat{r} + F_z \hat{z}$, where

$$F_r = \epsilon_0 \epsilon_r \frac{\partial \psi}{\partial r} \frac{\partial \psi}{\partial z} \tag{10}$$

$$F_z = \frac{\epsilon_0 \epsilon_r}{2} \left(\left(\frac{\partial \psi}{\partial z} \right)^2 - \left(\frac{\partial \psi}{\partial r} \right)^2 \right). \tag{11}$$

The interaction potential was then found by a path integral over the forces at various distances from the shell.

Van der Waals interaction

To calculate the vdW interaction between a sphere and a shell a relationship is required to determine the interaction between a sphere and an element located at a point a distance d away from the sphere surface.[81] By integrating over the shell volume we obtain the vdW interaction between a sphere and a shell at a distance d from the shell wall.

$$U_{\mathrm{vdW}}(d) = \frac{-16 A R_{\mathrm{core}}^3}{3} \int_0^{\pi} \int_{R_{\mathrm{core}}+d(\theta,a)}^{R_{\mathrm{core}}+d(\theta,a)+T_{\mathrm{shell}}} \frac{r^2 \sin(\theta) dr d\theta}{(r^2 - R_{\mathrm{core}}^2)^3} \tag{12}$$

Here A is the Hamaker constant, T_{shell} the thickness of the shell, r and θ the radial distance and polar angle in a spherical coordinate system. Finally, $d(\theta, a)$ is the distance of the core to different parts of the shell depending on the polar angle θ and the displacement from the

center of the shell a

$$d(\theta, a) = \sqrt{(R_{\text{shell}} - R_{\text{core}})^2 + a^2 \sin(\theta)^2} - a\cos(\theta). \tag{13}$$

R_{core} and R_{shell} are the radius of the core and the inner radius of the shell, respectively. For the titania@water@silica particles the used Hamaker constant was $A_{123} = 6.9\,\text{zJ}$, calculated via the full Lifshitz theory.[82] The used shell thickness was 25 nm. Equation 12 was integrated numerically in Mathematica.

Simulating static ADF-STEM images

To understand the influence of hydrodynamics and the errors in the measurements, we simulated ADF-STEM images of a moving particle within a shell. Therefore, we are first required to simulate ADF-STEM images for a static particle. For this purpose we simulated ADF-STEM images using the CASINO software (Version 3.3.0.4).[83–85] The physics model used for the total and partial cross sections in the simulation software was that of an empirical analytical fit to the Mott cross sections by Browning *et al.*[86] The specific parameters of the sample and the electron probe were taken to be as close to the experimental parameters as possible. However, we chose to use 256 by 256 pixels and twice the pixel size as in the experiments (which had 512 by 512 pixels) in order to reduce the computation time.

We put a 340 nm titania particle at different positions within a shell with a 700 nm inner diameter within a water layer of a micrometer. The electron probe was set to have a semi-convergence angle of 10 mrad and a diameter of 1 nm. The beam distribution was Gaussian. The electron probe had an energy of 200 keV and had its focal point on the middle of the rattle particle geometry. The top of the shell of the rattle geometry was at the same height as the top of the water layer. The pixel size was 8.9 nm and the number of simulated electrons per pixel N was 3528, as calculated from the beam current $I = 0.037\,\text{nA}$ and the pixel dwell

time $\tau = 1/256^2$ s via

$$N = \frac{I \cdot \tau}{e} \tag{14}$$

where e is the electron charge. The ADF detector with a quantum efficiency of 100% was set to have a minimum and maximum semi-angle of 15 and 300 mrad, respectively. In total 41 static images of a particle in different positions in the shell were simulated.

Simulating ADF-STEM images of a diffusing particle in a shell

We first calculated the diffusion coefficient of the particle in the shell. The diffusion coefficient of the particle depended on the position within the shell, as well as the direction of the displacement. The mobility of the core particle towards the shell (radial diffusion) and along the shell wall (perpendicular diffusion) was investigated using finite-element calculations. More details can be found in the Supporting Information.

When the directional diffusion coefficients at all positions of the core within the shell were known, the particle motion could be simulated. For every pixel that was scanned the particle was moved in a random direction with a velocity in the perpendicular and radial direction that was dependent on its current position within the shell. The random direction of the perpendicular vector v_p was coded by creating 2 normalized vectors v_1 and v_2 that were perpendicular to the radial direction, and choosing a random real number n_r between 0 and 2π. The direction of the perpendicular vector was then chosen using this random real number n_r via

$$v_p = v_1 \cos(n_r) + v_2 \sin(n_r) \tag{15}$$

Now that the direction of the radial displacement and the perpendicular displacement is decided, we let the particle move a random step, within the pixel dwell time Δt, in the radial and perpendicular directions based on a normal distribution with standard deviations σ_r and σ_p, respectively. These are related to the radial and perpendicular diffusion coefficients

D_r and D_p at the current position via

$$\sigma_r(r) = \sqrt{2D_r(r)\Delta t}, \tag{16}$$

$$\sigma_p(r) = \sqrt{4D_p(r)\Delta t}. \tag{17}$$

The particle was free to move up until a sharp barrier a certain distance away from the shell wall. When the new simulated position of the particle was not allowed by the imposed barrier, a new position of the particle was calculated from the old position until that new position was allowed.

When the position of the particle was known for every pixel scanned, the image of the moving particle was formed. This was achieved by taking the position of the particle at the time and finding the 3 static ADF-STEM images that included the core particle closest to that position. The pixel was then given an intensity based on the weighted mean of that same pixel in the 3 chosen ADF-STEM images. The mean was weighted linearly by the absolute distance of the particle position in the static image compared to the real position. This was done for every pixel in an image and for at least 180 images.

Author Contributions

TAJW performed the LC-STEM experiments, data analysis, the calculations, the simulations and wrote the manuscript. KW synthesized the rattle particles under supervision of DN. AGC helped with useful tips regarding the experimental data analysis. JdG helped set up the finite-element calculations and provided helpful advice on the theoretical side of the project. AI helped with the concept of flat potentials within the rattles. MAvH obtained the funding for the project and supervised the project. AvB supervised the project and co-wrote the manuscript. All authors have given approval for the final version of the manuscript.

Acknowledgement

We acknowledge Wessel Vlug for his early work on interactions within rattle-type particles. This project has received funding from the European Research Council (ERC) via the ERC Consolidator Grant NANO-INSITU (grant No. 683076). KW and DN acknowledge the support from the Ministry of Education, Culture, Sports, Science and Technology, Japan (Materials Processing Science project ("Materealize") of MEXT, Grant Number JPMXP0219192801). JdG thanks NWO for funding through Start-Up Grant No. 740.018.013 and through association with the EU-FET Project No. NANOPHLOW (766972) within Horizon 2020.

Supporting Information Available

The following files are available free of charge.

- Supporting Information. Synthesis details. Zeta potentials measurements. Volume corrections for the projected data. Extra details and checks on the calculations on electrostatic, van der Waals and hydrodynamic interactions. Influence of the electron beam. Estimation of the resolution.
- Movie S1: Titania@water@silica rattle-type particle in pure water at different electron dose rates. Electron dose rates shown in video in units of $e^{-}nm^{-2}s^{-1}$.
- Movie S2: Titania@water@silica rattle-type particle in 10.0 mM LiCl at different electron dose rates. Electron dose rates shown in video in units of $e^{-}nm^{-2}s^{-1}$.
- Movie S3: Titania@water@silica rattle-type particle at different pH. The electron dose rate was $95\,e^{-}nm^{-2}s^{-1}$.
- Movie S4: Gold@water@silica rattle-type particles at different pH. The electron dose rate was $179\,e^{-}nm^{-2}s^{-1}$.

- Movie S5: Gold@water@silica rattle-type particle in 1.00 mM LiCl at different electron dose rates. Electron dose rates shown in video in units of $e^{-}nm^{-2}s^{-1}$.

- Movie S6: Titania@water@silica rattle-type particle at various salt concentrations. The electron dose rate was $45\,e^{-}nm^{-2}s^{-1}$.

- Movie S7: Gold@water@silica rattle-type particle at various salt concentrations. The electron dose rate was $206\,e^{-}nm^{-2}s^{-1}$.

- Movie S8: Four gold@water@silica nanorattles. The top two gold particles are mobile. However, the particle in the middle is attached to the shell and only gets loose due to interactions with the electron beam. The bottom gold particle is mobile but the electron beam is causing it to sometimes stick to the shell wall for a frame. This shows that gold@void@silica nanorattles may sometimes be unstable in pure water due to a flat electric potential within the shell geometry. The electron dose rate was $206\,e^{-}nm^{-2}s^{-1}$.

References

1. Kamata, K.; Lu, Y.; Xia, Y. Synthesis and characterization of monodispersed core-shell spherical colloids with movable cores. *Journal of the American Chemical Society* **2003**, *125*, 2384–2385.

2. Priebe, M.; Fromm, K. M. Nanorattles or yolk-shell nanoparticles-what are they, how are they made, and what are they good for? *Chemistry - A European Journal* **2014**, *21*, 3854–3874.

3. Teng, Z.; Wang, S.; Su, X.; Chen, G.; Liu, Y.; Luo, Z.; Luo, W.; Tang, Y.; Ju, H.; Zhao, D.; Lu, G. Facile synthesis of yolk-shell structured inorganic-organic hybrid spheres with ordered radial mesochannels. *Advanced Materials* **2014**, *26*, 3741–3747.

4. Purbia, R.; Paria, S. Yolk/shell nanoparticles: Classifications, synthesis, properties, and applications. *Nanoscale* **2015**, *7*, 19789–19873.

5. Liu, J.; Qiao, S. Z.; Chen, J. S.; Lou, X. W.; Xing, X.; Lu, G. Q. Yolk/shell nanoparticles: New platforms for nanoreactors, drug delivery and lithium-ion batteries. *Chemical Communications* **2011**, *47*, 12578–12591.

6. Demirörs, A. F.; van Blaaderen, A.; Imhof, A. Synthesis of Eccentric Titania-Silica Core-Shell and Composite Particles. *Chem. Mater.* **2009**, 979–984.

7. Prieto, G.; Tüysüz, H.; Duyckaerts, N.; Knossalla, J.; Wang, G. H.; Schüth, F. Hollow Nano- and Microstructures as Catalysts. *Chemical Reviews* **2016**, *116*, 14056–14119.

8. Nagao, D.; van Kats, C. M.; Hayasaka, K.; Sugimoto, M.; Konno, M.; Imhof, A.; van Blaaderen, A. Synthesis of hollow asymmetrical silica dumbbells with a movable inner core. *Langmuir* **2010**, *26*, 5208–5212.

9. Watanabe, K.; Ishii, H.; Konno, M.; Imhof, A.; van Blaaderen, A.; Nagao, D. Yolk/shell colloidal crystals incorporating movable cores with their motion controlled by an external electric field. *Langmuir* **2017**, *33*, 296–302.

10. Okada, A.; Nagao, D.; Ueno, T.; Ishii, H.; Konno, M. Colloidal polarization of yolk/shell particles by reconfiguration of inner cores responsive to an external magnetic field. *Langmuir* **2013**, *29*, 9004–9009.

11. Tan, L.; Chen, D.; Liu, H.; Tang, F. A silica nanorattle with a mesoporous shell: An ideal nanoreactor for the preparation of tunable gold cores. *Advanced Materials* **2010**, *22*, 4885–4889.

12. da Silva, A. G.; Rodrigues, T. S.; Correia, V. G.; Alves, T. V.; Alves, R. S.; Ando, R. A.; Ornellas, F. R.; Wang, J.; Andrade, L. H.; Camargo, P. H. Plasmonic Nanorattles as

Next-Generation Catalysts for Surface Plasmon Resonance-Mediated Oxidations Promoted by Activated Oxygen. *Angewandte Chemie - International Edition* **2016**, *55*, 7111–7115.

13. Lee, J.; Park, J. C.; Song, H. A Nanoreactor framework of a Au@SiO_2 yolk/shell structure for catalytic reduction of p-nitrophenol. *Advanced Materials* **2008**, *20*, 1523–1528.

14. Kuo, C. H.; Tang, Y.; Chou, L. Y.; Sneed, B. T.; Brodsky, C. N.; Zhao, Z.; Tsung, C. K. Yolk-shell nanocrystal@ZIF-8 nanostructures for gas-phase heterogeneous catalysis with selectivity control. *Journal of the American Chemical Society* **2012**, *134*, 14345–14348.

15. Wang, X.; He, Y.; Ma, Y.; Liu, J.; Liu, Y.; Qiao, Z. A.; Huo, Q. Architecture of yolk-shell structured mesoporous silica nanospheres for catalytic applications. *Dalton Transactions* **2018**, *47*, 9072–9078.

16. Wu, S.; Dzubiella, J.; Kaiser, J.; Drechsler, M.; Guo, X.; Ballauff, M.; Lu, Y. Thermosensitive Au-PNIPA yolk-shell nanoparticles with tunable selectivity for catalysis. *Angewandte Chemie - International Edition* **2012**, *51*, 2229–2233.

17. Fan, L.; Xu, X.; Zhu, C.; Han, J.; Gao, L.; Xi, J.; Guo, R. Tumor Catalytic-Photothermal Therapy with Yolk-Shell Gold@Carbon Nanozymes. *ACS Applied Materials and Interfaces* **2018**, *10*, 4502–4511.

18. Lin, L. S.; Song, J.; Yang, H. H.; Chen, X. Yolk–Shell Nanostructures: Design, Synthesis, and Biomedical Applications. *Advanced Materials* **2018**, *30*, 1–30.

19. Zhang, L.; Wang, T.; Yang, L.; Liu, C.; Wang, C.; Liu, H.; Wang, Y. A.; Su, Z. General route to multifunctional uniform yolk/mesoporous silica shell nanocapsules: A platform for simultaneous cancer-targeted imaging and magnetically guided drug delivery. *Chemistry - A European Journal* **2012**, *18*, 12512–12521.

20. Du, P.; Liu, P. Novel smart yolk/shell polymer microspheres as a multiply responsive cargo delivery system. *Langmuir* **2014**, *30*, 3060–3068.

21. Roca, M.; Haes, A. J. Silica-void-gold nanoparticles: Temporally stable surface-enhanced raman scattering substrates. *Journal of the American Chemical Society* **2008**, *130*, 14273–14279.

22. Shrestha, B. K.; Haes, A. J. Improving surface enhanced Raman signal reproducibility using gold-coated silver nanospheres encapsulated in silica membranes. *Journal of Optics (United Kingdom)* **2015**, *17*, 0–18.

23. Wang, H.; Xu, R.; Chen, H.; Yuan, Q. Synthesis of nitrogen and sulfur co-doped yolk-shell porous carbon microspheres and their application for Pb(II) detection in fish serum. *Journal of Solid State Chemistry* **2018**, *266*, 63–69.

24. Rai, P.; Yoon, J. W.; Jeong, H. M.; Hwang, S. J.; Kwak, C. H.; Lee, J. H. Design of highly sensitive and selective Au@NiO yolk-shell nanoreactors for gas sensor applications. *Nanoscale* **2014**, *6*, 8292–8299.

25. Watanabe, K.; Welling, T. A. J.; Sadighikia, S.; Ishii, H.; Imhof, A.; van Huis, M. A.; van Blaaderen, A.; Nagao, D. Compartmentalization of gold nanoparticle clusters in hollow silica spheres and their assembly induced by an external electric field. *Journal of Colloid and Interface Science* **2020**, *566*, 202–210.

26. Pan, S.; Li, J.; Wan, G.; Liu, C.; Fan, W.; Wang, L. Nanosized yolk-shell Fe_3O_4@$Zr(OH)_x$ spheres for efficient removal of Pb(II) from aqueous solution. *Journal of Hazardous Materials* **2016**, *309*, 1–9.

27. Zhao, L.; Liu, H.; Wang, F.; Zeng, L. Design of yolk-shell Fe_3O_4@PMAA composite microspheres for adsorption of metal ions and pH-controlled drug delivery. *Journal of Materials Chemistry A* **2014**, *2*, 7065–7074.

28. Wu, C.; Tong, X.; Ai, Y.; Liu, D. S.; Yu, P.; Wu, J.; Wang, Z. M. A Review: Enhanced Anodes of Li/Na-Ion Batteries Based on Yolk-Shell Structured Nanomaterials. *Nano-Micro Letters* **2018**, *10*, 1–18.

29. de Jonge, N.; Ross, F. M. Electron microscopy of specimens in liquid. *Nature Nanotechnology* **2011**, *103*, 163–164.

30. Ross, F. M. Opportunities and challenges in liquid cell electron microscopy. *Science* **2015**, *350*, aaa9886.

31. de Jonge, N. Theory of the spatial resolution of (scanning) transmission electron microscopy in liquid water or ice layers. *Ultramicroscopy* **2018**, *187*, 113–125.

32. Welling, T. A. J.; Sadighikia, S.; Watanabe, K.; Grau-Carbonell, A.; Bransen, M.; Nagao, D.; van Blaaderen, A.; van Huis, M. A. Observation of Undamped 3D Brownian Motion of Nanoparticles Using Liquid-Cell Scanning Transmission Electron Microscopy. *Particle & Particle Systems Characterization* **2020**, *37*, 2000003.

33. Yesibolati, M. N.; Mortensen, K. I.; Sun, H.; Brostrøm, A.; Tidemand-Lichtenberg, S.; Mølhave, K. Unhindered Brownian Motion of Individual Nanoparticles in Liquid-Phase Scanning Transmission Electron Microscopy. *Nano Letters* **2020**, *20*, 7108–7115.

34. Chen, Q.; Cho, H.; Manthiram, K.; Yoshida, M.; Ye, X.; Alivisatos, A. P. Interaction Potentials of Anisotropic Nanocrystals from the Trajectory Sampling of Particle Motion using in Situ Liquid Phase Transmission Electron Microscopy. *ACS Central Science* **2015**, *1*, 150323114811004.

35. Powers, A. S.; Liao, H.-G.; Raja, S. N.; Bronstein, N. D.; Alivisatos, A. P.; Zheng, H. Tracking Nanoparticle Diffusion and Interaction during Self-Assembly in a Liquid Cell. *Nano Letters* **2017**, *17*, 15–20.

36. Derjaguin, B. V. On the repulsive forces between charged colloid particles and on the theory of slow coagulation and stability of lyophobe sols. *Transactions of the Faraday Society* **1940**, *35*, 203–215.

37. Verwey, E.; Overbeek, J. *Theory of Stability of Lyophobic Colloids*; Elsevier: Amsterdam, 1948.

38. Verwey, E. J. W.; Overbeek, J. T. G.; Van Nes, K. *Theory of the stability of lyophobic colloids: the interaction of sol particles having an electric double layer*; Elsevier Publishing Company, 1948.

39. Israelachvili, J. *Intermolecular and Surface Forces*, 3rd ed.; Academic Press: London, 2011.

40. Russel, W. B.; Saville, D. A.; Schowalter, W. *Colloidal Dispersions*; Cambridge University Press, 1989.

41. Hansen, J.-P.; Löwen, H. Effective interactions between electric double layers. *Annual Review of Physical Chemistry* **2000**, *52*, 209–242.

42. Liang, Y.; Hilal, N.; Langston, P.; Starov, V. Interaction forces between colloidal particles in liquid: Theory and experiment. *Advances in Colloid and Interface Science* **2007**, *134-135*, 151–166.

43. Min, Y.; Akbulut, M.; Kristiansen, K.; Golan, Y.; Israelachvili, J. The role of interparticle and external forces in nanoparticle assembly. *Nanoscience and Technology: A Collection of Reviews from Nature Journals* **2009**, 38–49.

44. Silvera Batista, C.; Larson, R.; Kotov, N. Nonadditivity of nanoparticle interactions. *Science* **2015**, *350*, 1242477.

45. Walker, D. A.; Kowalczyk, B.; De La Cruz, M. O.; Grzybowski, B. A. Electrostatics at the nanoscale. *Nanoscale* **2011**, *3*, 1316–1344.

46. Dahirel, V.; Jardat, M. Effective interactions between charged nanoparticles in water: What is left from the DLVO theory? *Current Opinion in Colloid and Interface Science* **2010**, *15*, 2–7.

47. Avni, Y.; Komura, S.; Andelman, D. Brownian motion of a charged colloid in restricted confinement. *arXiv preprint arXiv:2012.07070* **2020**,

48. Dufresne, E. R.; Altman, D.; Grier, D. G. Brownian dynamics of a sphere between parallel walls. *Europhysics Letters* **2001**, *53*, 264–270.

49. Klokkenburg, M.; Dullens, R. P.; Kegel, W. K.; Erné, B. H.; Philipse, A. P. Quantitative real-space analysis of self-assembled structures of magnetic dipolar colloids. *Physical Review Letters* **2006**, *96*, 037203.

50. van Rijssel, J.; van Der Linden, M.; Meeldijk, J. D.; van Dijk-Moes, R. J. A.; Philipse, A. P.; Erné, B. H. Spatial distribution of nanocrystals imaged at the liquid-air interface. *Physical Review Letters* **2013**, *111*, 1–5.

51. Bradac, C. Nanoscale Optical Trapping: A Review. *Advanced Optical Materials* **2018**, *6*, 1800005.

52. Grier, D. G. A revolution in optical manipulation. *Nature* **2003**, *424*, 810–816.

53. Masri, D. E.; van Oostrum, P.; Smallenburg, F.; Vissers, T.; Imhof, A.; Dijkstra, M.; van Blaaderen, A. Measuring colloidal forces from particle position deviations inside an optical trap. *Soft Matter* **2011**, *7*, 3462–3466.

54. Royall, C. P.; Leunissen, M. E.; van Blaaderen, A. A new colloidal model system to study long-range interactions quantitatively in real space. *Journal of Physics: Condensed Matter* **2003**, *15*, S3581–S3596.

55. Butt, H.-J.; Cappella, B.; Kappl, M. Force measurements with the atomic force microscope: Technique, interpretation and applications. *Surface Science Reports* **2005**, *59*, 1–152.

56. Yethiraj, A.; van Blaaderen, A. A colloidal model system with an interaction tunable from hard sphere to soft and dipolar. *Nature* **2003**, *421*, 513–517.

57. Albers, W.; Overbeek, J. T. G. Stability of emulsions of water in oil. I. The correlation between electrokinetic potential and stability. *Journal of Colloid Science* **1959**, *14*, 501–509.

58. Albers, W.; Overbeek, J. T. G. Stability of emulsions of water in oil. II. Charge as a factor of stabilization against flocculation. *Journal of Colloid Science* **1959**, *14*, 510–518.

59. Mishchuk, N. A.; Sanfeld, A.; Steinchen, A. Interparticle interactions in concentrate water–oil emulsions. *Advances in Colloid and Interface Science* **2004**, *112*, 129–157.

60. Sainis, S. K.; Merrill, J. W.; Dufresne, E. R. Electrostatic interactions of colloidal particles at vanishing ionic strength. *Langmuir* **2008**, *24*, 13334–13337.

61. Gillespie, D. A.; Hallett, J. E.; Elujoba, O.; Che Hamzah, A. F.; Richardson, R. M.; Bartlett, P. Counterion condensation on spheres in the salt-free limit. *Soft Matter* **2014**, *10*, 566–577.

62. Merrill, J. W.; Sainis, S. K.; Dufresne, E. R. Many-Body Electrostatic Forces between Colloidal Particles at Vanishing Ionic Strength. *Physical Review Letters* **2009**, *103*, 138301.

63. Finlayson, S. D.; Bartlett, P. Non-additivity of pair interactions in charged colloids. *Journal of Chemical Physics* **2016**, *145*, 034905.

64. Cervantes-Martínez, A. E.; Ramírez-Saito, A.; Armenta-Calderón, R.; Ojeda-López, M. A.; Arauz-Lara, J. L. Colloidal diffusion inside a spherical cell. *Physical Review E - Statistical, Nonlinear, and Soft Matter Physics* **2011**, *83*, 1–4.

65. Aponte-Rivera, C.; Zia, R. N. Simulation of hydrodynamically interacting particles confined by a spherical cavity. *Physical Review Fluids* **2016**, *1*, 023301.

66. Eichmann, S. L.; Anekal, S. G.; Bevan, M. A. Electrostatically confined nanoparticle interactions and dynamics. *Langmuir* **2008**, *24*, 714–721.

67. Watanabe, K.; Kuroda, K.; Nagao, D. Polyethylenimine-assisted synthesis of hollow silica spheres without shape deformation. *Materials Chemistry and Physics* **2021**, *262*, 124267.

68. Grau-Carbonell, A.; Sadighikia, S.; Welling, T. A. J.; van Dijk-Moes, R. J. A.; Kotni, R.; Bransen, M.; van Blaaderen, A.; van Huis, M. A. In Situ Study of the Wet Chemical Etching of SiO_2 and Nanoparticle@SiO_2 Core–Shell Nanospheres. *ACS Applied Nano Materials* **2021**, *4*, 1136–1148.

69. Schneider, N. M.; Norton, M. M.; Mendel, B. J.; Grogan, J. M.; Ross, F. M.; Bau, H. H. Electron-Water interactions and implications for liquid cell electron microscopy. *Journal of Physical Chemistry C* **2014**, *118*, 22373–22382.

70. Zheng, H.; Claridge, S. A.; Minor, A. M.; Alivisatos, A. P.; Dahmen, U. Nanocrystal diffusion in a liquid thin film observed by in situ transmission electron microscopy. *Nano Letters* **2009**, *9*, 2460–2465.

71. Tadros, T. F.; Lyklema, J. Adsorption of potential-determining ions at the silica-aqueous electrolyte interface and the role of some cations. *Journal of Electroanalytical Chemistry and Interfacial Electrochemistry* **1968**, *17*, 267–275.

72. Sverjensky, D. A. Prediction of surface charge on oxides in salt solutions: Revisions for 1:1 (M^+L^-) electrolytes. *Geochimica et Cosmochimica Acta* **2005**, *69*, 225–257.

73. Kobayashi, M.; Juillerat, F.; Galletto, P.; Bowen, P.; Borkovec, M. Aggregation and charging of colloidal silica particles: Effect of particle size. *Langmuir* **2005**, *21*, 5761–5769.

74. Vakarelski, I. U.; Teramoto, N.; McNamee, C. E.; Marston, J. O.; Higashitani, K. Ionic enhancement of silica surface nanowear in electrolyte solutions. *Langmuir* **2012**, *28*, 16072–16079.

75. Hallez, Y.; Meireles, M. Modeling the Electrostatics of Hollow Shell Suspensions: Ion Distribution, Pair Interactions, and Many-Body Effects. *Langmuir* **2016**, *32*, 10430–10444.

76. Behrens, S. H.; Grier, D. G. Pair interaction of charged colloidal spheres near a charged wall. *Physical Review E* **2001**, *64*, 050401.

77. Richardson, W. H. Bayesian-Based Iterative Method of Image Restoration. *Journal of the Optical Society of America* **1972**, *62*, 55.

78. Lucy, L. B. An iterative technique for the rectification of observed distributions. *The Astronomical Journal* **1974**, *79*, 745.

79. Rempfer, G.; Davies, G. B.; Holm, C.; De Graaf, J. Reducing spurious flow in simulations of electrokinetic phenomena. *Journal of Chemical Physics* **2016**, *145*.

80. Rempfer, G.; Ehrhardt, S.; Holm, C.; de Graaf, J. Nanoparticle Translocation through Conical Nanopores: A Finite Element Study of Electrokinetic Transport. *Macromolecular Theory and Simulations* **2017**, *26*, 1–14.

81. Troncoso, A. B.; Acosta, E. The van der Waals interactions in sphere-shell and cone-shell configurations. *Journal of Physical Chemistry B* **2012**, *116*, 14051–14061.

82. Bergström, L. Hamaker constants of inorganic materials. *Advances in Colloid and Interface Science* **1997**, *70*, 125–169.

83. Drouin, D.; Couture, A. R.; Joly, D.; Tastet, X.; Aimez, V.; Gauvin, R. CASINO V2.42 A Fast and Easy-to-use Modeling Tool for Scanning Electron Microscopy and Microanalysis Users. *Scanning* **2007**, *29*, 92–101.

84. Demers, H.; Poirier-Demers, N.; Couture, A. R.; Joly, D.; Guilmain, M.; de Jonge, N.; Drouin, D. Three-dimensional electron microscopy simulation with the CASINO Monte Carlo software. *Scanning* **2011**, *33*, 135–146.

85. Poirier-Demers, N.; Demers, H.; Drouin, D.; de Jonge, N. Simulating STEM Imaging of Nanoparticles in Micrometers-Thick Substrates. *Microscopy and Microanalysis* **2011**, *17*, 980–981.

86. Browning, R.; Li, T. Z.; Chui, B.; Ye, J.; Pease, R. F.; Czyzewski, Z.; Joy, D. C. Empirical forms for the electron/atom elastic scattering cross sections from 0.1 to 30 keV. *Journal of Applied Physics* **1994**, *76*, 2016–2022.

TOC Graphic

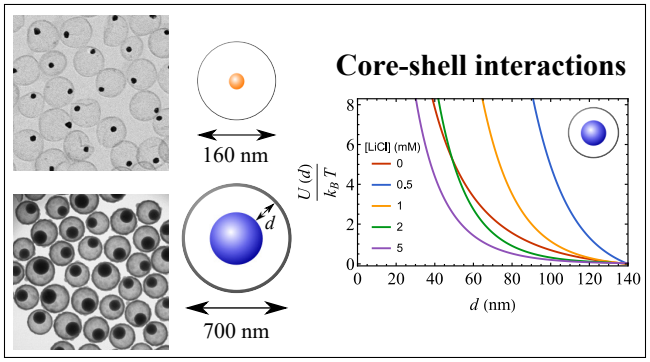
160 nm
d
700 nm
Core-shell interactions
U (d) / k_B T
[LiCl] (mM)
0
0.5
1
2
5
0
2
4
6
8
0
20
40
60
80
100
120
140
d (nm)